PHYSICAL REVIEW FLUIDS **9**, 034305 (2024)

Turbophoresis and preferential accumulation of inertial particles in compressible turbulent channel flow: Effect of Mach number

Ping Wang,[1] Bowen Zhou,[1] and Xiaojing Zheng[2,*]
[1] *Key Laboratory of Mechanics on Disaster and Environment in Western China, Ministry of Education of China, Department of Mechanics, Lanzhou University, Lanzhou 730000, China*
[2] *Research Center for Applied Mechanics, School of Mechano-Electronic Engineering, Xidian University, Xi'an 710071, China*

(Received 14 December 2023; accepted 1 March 2024; published 21 March 2024)

Direct numerical simulations of channel turbulence laden with inertial particles were performed to investigate the effects of the Mach number on turbophoresis and the preferential accumulation of particles using the Eulerian-Lagrangian point-particle method. The results show that turbophoresis-induced particle segregation is suppressed at high Mach number. A particle relaxation time weighting transformation is proposed which collapses the concentration profiles not only for particles with small inertia but also for turbulence with various compressibility at the studied low Reynolds number and in the inner region. The conditional sampling reveals that inertial particles in compressible wall turbulence tend to distribute in low-fluid-speed regions near the wall and high-fluid-speed regions in the outer layer, which is similar to that in incompressible turbulence. What is special is that they also tend to distribute in high-fluid-density and negative-fluid-dilatation regions. This is explained by the changes in turbulent structures at varying Mach number, which in turn also account for the varying scales of particle streaks.

DOI: 10.1103/PhysRevFluids.9.034305

I. INTRODUCTION

Compressible turbulent particle-laden flow has a wide range of engineering and environmental applications, such as fuel mixing in scramjet engines, deposition of ash on turbine blades, and the exhaust of rocket engines [1–4]. It is also commonly experienced by aircraft when flying in rainy or sandy environments (on Earth or Mars) [5,6]. Particle dispersion and accumulation in particle-laden turbulent flow, driven by the flow statistics and the action of coherent structures, are crucial because they directly affect the momentum and energy transfer between particles and the fluid [7,8]. The compressibility effects due to the nonlinear interaction among velocity, pressure, and temperature field, as well as the shocklets, will further increase the complexity of particle behavior [9,10]. Therefore, research studies on particle dispersion and accumulation in compressible two-phase flow at various Mach number (Ma) are of great importance.

Investigations on the particle dispersion and accumulation in particle-laden flow have been thoroughly documented in the past several decades. The reader is referred to [1,11] for the state-of-the-art progress. The majority of these studies are for incompressible turbulence and based on simple flow geometries, such as homogeneous isotropic turbulence, pipe flow, channel flow, and spatially developing boundary layers [12–15]. For the motion of inertial particles in wall-bounded turbulence, the direct numerical simulation (DNS) in the Euler-Lagrangian framework [14,16–20]

*xjzheng@lzu.edu.cn

is the most frequently used approach to investigate the particle dynamics and the mechanisms since experimental observations of particle concentration in the near-wall region are extremely difficult [21]. These studies have revealed that turbophoresis is a key process for the dispersion and accumulation of inertial particles. Due to turbophoresis, small and heavy particles tend to migrate from high- to low-turbulent-intensity regions [22,23]. The no-slip conditions of wall-bounded turbulence lead to the disappearing turbulent intensity at the solid boundary and generate a sharp gradient of turbulent intensity in the viscous sublayer. Therefore, particles tend to accumulate there [24,25], accompanying a nonuniform particle distribution in the wall-normal direction. Note that turbophoresis is a statistical theory interpreting the overall fluxes of particles toward and away from the wall and also understood as the joint effects of particle inertia and the dynamics of the turbulence structures (ejection/sweeping event) populating the near-wall region [24]. The turbophoresis-induced particle segregation exhibits the Stokes number effects. For example, the results of the particle-laden channel flow simulated by Bernardini [18] indicate that strong particle segregation is observed in the near-wall region within the range of $\mathrm{St}^+ = 10$–100. At least in the range of $\mathrm{Re}_\tau = 150$–1000, the wall-normal concentration profiles collapse in inner scaling. However, outside this St^+ range, particles are relatively uniform distributed along the wall-normal direction and the scaling law is unclear. Here the friction Reynolds number Re_τ is defined as the ratio of the outer scale h to the viscous length scale δ_ν, where $\delta_\nu = \nu/u_\tau$, ν is the kinematic viscosity of the fluid and u_τ is the friction velocity. St^+ is the ratio of the particle relaxation time $\tau_p = \rho_p d_p^2/18\mu$ to the fluid viscous timescale τ_f. Here ρ_p and d_p are the particle density and diameter, respectively, and $\mu = \rho\nu$ is the dynamic viscosity of the fluid.

Another important phenomenon observed in turbulent multiphase flow is the preferential accumulation, namely, particles are unable to completely follow the fluid trajectory and cluster locally due to inertia [26]. This localized accumulation is often highly related to the spatial structure of the surrounding fluid [27]. Low-inertia particles tend to be thrown out from the vortex core due to the centrifugal effects [12] and are distributed outside the vortex structure [21] in homogeneous isotropic turbulence. The spatial distribution of high-inertia particles cannot be only determined by the instantaneous flow field. Instead, the history effects also need to be taken into account [28–31]. For the wall-bounded turbulent flow, inertial particles are found preferentially stay in the regions of negative streamwise velocity fluctuations near the wall [13,24,32–34] due to the near-wall sweeps and ejections, forming small-scale particle streaks. This tendency is observed most significantly for the Stokes number range of $\mathrm{St}^+ = O(1)$–$O(10)$. The average spanwise spacing of particle streaks is about 120 viscous units [35], and the streamwise length scale is approximately $500 \sim 1000$ viscous units [36] in low-Reynolds-number turbulent channel flows. Recently, Wang and Richter [37] and Jie *et al.* [38] ound that inertial particles also exhibit large-scale organized structures in the outer region of turbulent channel flow at moderate to high Reynolds numbers. The observed large-scale particle streaks for relatively high-inertia particles [$\mathrm{St}^+ = O(100)$] are related to large-scale turbulent motions, indicating that particles with different inertia respond efficiently to turbulent structures with similar timescales.

Compressible and incompressible flow share the similarities in the near-wall structures [39], large-scale motions [40], and wall pressure coherence [41], etc. However, compressible turbulence also differs from incompressible turbulence in many aspects, such as larger turbulent dissipation [42], more suppressed turbulent intensity [43], the presence of the wall temperature effects [44], and the shocklets [45]. Studies on compressible particle-laden flow have revealed some important characteristics of particle motion, dispersion, and preferential accumulation [2,9,10,20,26,27,45]. For example, in low-turbulent-Mach-number [M_t, defined as $M_t = (\overline{u_i' u_i'})^{1/2}/\bar{a}$, where u_i' is the velocity fluctuation component obtained from the Reynolds decomposition, a is the local speed of sound, and "$-$" represents the Reynolds averaging operation] homogeneous isotropic turbulence, particles also tend to preferentially accumulate in low-vorticity regions of the margin of vortex structure. This phenomenon is the strongest when $\mathrm{St}_\eta \sim O(1)$ [30,46], where St_η is the Stokes number based on the Kolmogorov timescale of turbulence [12]. As the Mach number increases, however, the accumulation of particles in low-vorticity regions is slightly reduced. Meanwhile, an interesting new phenomenon was observed by Zhang *et al.* [27] that particles have a tendency to accumulate in high-density regions of the flow field and the moderate-/high-inertia particles may accumulate in high-vorticity regions behind the randomly formed shocklets if $M_t > 1$. Li and Bai [10] studied the behavior of microparticles in a two-dimensional supersonic laminar boundary layer and revealed three different patterns of particle motion and the main determining parameters involved. Li and Bai [2] found that particles tend to move towards the wall with increasing gravity and Mach number, as well as decreasing initial wall-normal distance. Teh and Johansen [47] studied the interaction between solid particles and laminar boundary layers through numerical simulations and found that particles can suppress flow separation. Xiao *et al.* [26] performed DNSs of spatially developing compressible turbulent boundary layer at free-stream Mach number of 2.0 for particles with $\mathrm{St}^+ = 24.33$ and 2.36. The particle statistics and preferential concentration were found to be similar to those in the incompressible wall-bounded particle-laden flow. Apart from the low-vorticity-region accumulation, they also discovered a new mechanism for particle preferential accumulation, that high-inertia particles tend to accumulate in low-density regions in the inner region and high-density regions in the outer region while low-inertia particles still remain in low-density regions.

Nevertheless, research on compressible particle-laden flow is still insufficient. In this study, we focus on the dispersion behaviors of particles in wall-bounded compressible turbulence. The direct numerical simulation within an Euler-Lagrangian point-particle framework is employed to investigate the turbophoresis and the preferential concentration of inertial particles at various Mach number (0.8, 1.5, and 2.0). Since Xiao *et al.* [26] have demonstrated that inertial particles exhibit the most obvious segregation phenomenon in compressible wall turbulence in the range of $\mathrm{St}^+ = O(1)$–$O(10)$, the inner-scale particle Stokes numbers in the simulation are set to 0.72–10.8. This paper is organized as follows: in Sec. II, we describe the nondimensional parameters, governing equations for the fluid and particles, and the numerical scheme and simulation details. The turbophoresis and the preferential accumulation of particles are presented in Sec. III. Finally, conclusions are given in Sec. IV.

II. NUMERICAL METHODOLOGY

A. Governing equations for the fluid phase

We simulate the compressible two-phase flow in a channel. The open source code OpenCFD [48] is employed to calculate the carrier phase. This finite difference code has been used to successfully simulate compressible channel flow, homogeneous isotropic turbulence, boundary layers [48–50], etc. The fluid is assumed to be a Newtonian fluid that satisfies the continuity equation, the compressible Navier-Stokes equations, and the energy conservation equation. These dimensionless governing equations are

$$\frac{\partial \rho}{\partial t} + \frac{\partial(\rho u_j)}{\partial x_j} = 0, \tag{1}$$

$$\frac{\partial(\rho u_i)}{\partial t} + \frac{\partial}{\partial x_j}\left(\rho u_i u_j + p_m \delta_{ij} - \frac{1}{\mathrm{Re}}\sigma_{ij}\right) = 0, \tag{2}$$

$$\frac{\partial e}{\partial t} + \frac{\partial}{\partial x_j}\left[(e + p_m)u_j - \frac{1}{\mathrm{Re}}u_i\sigma_{ij} - \frac{1}{\mathrm{PrRe}(\gamma - 1)\mathrm{Ma}^2}\left(k\frac{\partial T}{\partial x_j}\right)\right] = 0. \tag{3}$$

It is the ideal gas and satisfies the state equation

$$p = \rho T, \tag{4}$$

where ρ is density, u_j is the velocity component, x_j is the Cartesian coordinate in the jth direction, and $j = 1, 2, 3$ represents the streamwise (x), wall-normal (y), and spanwise (z) direction, respectively. The origin of the y coordinate is at the centerline of the channel. $p_m = p/\gamma \mathrm{Ma}^2$ is the dimensionless modified pressure, t is time, T is temperature, and e is the total energy per unit volume

$$e = \frac{1}{2}\rho u_i u_i + \frac{p_m}{\gamma - 1}. \tag{5}$$

The specific heat ratio $\gamma = C_p/C_v$ is the ratio of the specific heat at constant pressure C_p to that at constant volume C_v. σ_{ij} is the viscous stress tensor, which can be expressed as

$$\sigma_{ij} = 2\mu\left(S_{ij} - \tfrac{1}{3}S_{kk}\delta_{ij}\right). \tag{6}$$

$S_{ij} = (\partial u_i/\partial x_j + \partial u_j/\partial x_i)/2$ is the strain-rate tensor. For compressible air, the dynamic viscosity μ is a function of temperature and calculated using the Sutherland equation [51]

$$\mu = \mu_w \frac{1 + S/T_{\mathrm{ref}}}{T + S/T_{\mathrm{ref}}} T^{\frac{3}{2}}, \tag{7}$$

where μ_w is the dynamic viscosity on the wall, and S and T_{ref} are reference quantities [52]. Pr, Ma, and Re are the Prandtl number, Mach number, and Reynolds number, respectively, and will be defined in the next subsection. Note that we perform only one-way coupling simulation and neglect the modulation of flow by the presence of particles. Therefore, the governing equations of the flow do not include particle feedback. Equations (1)–(3) are discretized using an eighth-order central scheme for the viscous terms. The time integration is achieved using a third-order Runge-Kutta method. An important aspect in compressible turbulence is that the shocklets may occur when the turbulent Mach number M_t is high enough. In such cases, shock-capturing methods (such as WENO schemes or TVD limiters) are necessary to capture the flow discontinuities [53,54]. In this context, we utilize an optimized seventh-order Weighted Essentially Nonoscillatory (WENO-7) scheme [55] to discretize the convective terms described in Eqs. (1)–(3). Periodic boundary conditions are imposed in the streamwise and spanwise directions. No-slip and isothermal conditions are employed for velocities and temperature at the solid boundaries. The random perturbations are superposed on the initial laminar velocity profiles to accelerate transition. The density and temperature are initially uniform [56].

B. Lagrangian particle tracking

The Lagrangian particle-tracking method is used to calculate the particle motion, which is governed only by the drag force. The shear and rotation lift forces, pressure gradient force, Basset force, virtual mass force, and other unsteady forces are all ignored due to the small size of the studied spherical solid particle and high particle-to-fluid density ratio. We discuss the dispersion of dilute (low particle volume fraction) point particles in compressible turbulence and hence neglect the interactions between particles [57]. This approach has been widely used in previous works [19,26,45,58] and enables comparisons with existing results. The drag force is calculated according to Schiller and Naumann [59], and the governing equations for particle motion can be written as

$$\frac{dx_{p,i}}{dt} = u_{p,i}, \tag{8}$$

$$\frac{du_{p,i}}{dt} = \frac{\left(1 + 0.15\mathrm{Re}_p^{0.687}\right)}{\tau_p}(v_{p,i} - u_{p,i}), \tag{9}$$

where $x_{p,i}$ and $u_{p,i}$ represent the position and velocity of particle. $v_{p,i}$ denotes the fluid velocity at the particle position $x_{p,i}$. $\mathrm{Re}_p = \rho_p|\mathbf{u}_p - \mathbf{v}_p|d_p/\mu_p$ is the particle slip Reynolds number based on the magnitude of the slip velocity vector $|\mathbf{u}_p - \mathbf{v}_p|$, and μ_p is the local fluid dynamic viscosity at $x_{p,i}$. ρ_p is the density of particles. $\tau_p = \rho_p d_p^2/18\mu_p$ is the local particle relaxation time at particle position $x_{p,i}$. In addition, since the slip Mach number Ma_p (defined as $\mathrm{Ma}_p = |\mathbf{u}_p - \mathbf{v}_p|/a_p$, where a_p is the sound speed at $x_{p,i}$) for 99.9% of the tracked particles are less than 0.4, the compressibility correction to the drag force is neglected [60].

After achieving the statistical steady state of the turbulence simulation, the inertial particles are released into the flow field with zero-slip initial velocities [18]. The equations of particle motion are then solved using the third-order Runge-Kutta method with the same time step as the fluid, ensuring that the particle CFL number is less than 0.1. Periodic boundary conditions are used in both the streamwise and spanwise directions. The particles experience perfect elastic collision when they contact the top and bottom solid wall. The fluid and flow information at the particle position are calculated by trilinear interpolation method [18,26].

C. Computational parameters and validation

In a compressible turbulence, the physical properties of the fluid vary with time and space. The dimensionless parameters of particles will change along their trajectories as well. It is hence essential to determine the dimensionless parameters that remain invariant in the two-phase flow for the numerical simulations and the following discussions. Since the channel flow is driven by a constant mass-flow rate and over isothermal walls, the bulk velocity U_b, the bulk density ρ_b, the half-width of the channel h, and the wall temperature T_w are all constants. Therefore, the dynamic viscosity at the wall μ_w is constant according to Eq. (7). In Eqs. (2) and (3), the Reynolds number and Mach number are defined as $\mathrm{Re} = \rho_b U_b h/\mu_w$ and $\mathrm{Ma} = U_b/a_w$, respectively, with the sound speed $a_w = \sqrt{\gamma R T_w}$. Accordingly, the outer-scale particle Stokes number St defined as $\mathrm{St} = \tau_{p,w}/\tau_f^{\mathrm{out}}$ could be constant for given particle size and density, where $\tau_f^{\mathrm{out}} = h/U_b$ is the outer-scale characteristic time of turbulence and $\tau_{p,w} = \rho_p d_p^2/18\mu_w$ is the particle relaxation time at the wall. In the present study, both the Reynolds (represented by $\bar{\phi}$ for an arbitrary quantity ϕ) and the Favre averaging ($\tilde{\phi} = \overline{\rho\phi}/\bar{\phi}$) are employed and conducted over the wall-parallel directions and time. The inner-scale quantities of compressible flow are denoted by the subscript "+," such as $\bar{u}^+ = \bar{u}/u_\tau$, where the friction velocity at the wall is $u_\tau = \sqrt{\bar{\tau}_w/\bar{\rho}_w}$, and $\bar{\tau}_w = \overline{\mu du/dy}|_w$. Analogously, $y^+ = y/\delta_\nu$, where $\delta_\nu = \bar{\rho}_w \mu_w/u_\tau$, and $\mathrm{St}^+ = \tau_{p,w}/t_\nu$, where $t_\nu = \delta_\nu/u_\tau$. We emphasize again that the quantities on the wall are denoted by a lowercase "w."

The computational domain is $L_x \times L_y \times L_z = 6\pi h \times 2h \times 2\pi h$ and the number of grid points is $N_x \times N_y \times N_z = 512 \times 129 \times 256$ in the streamwise, wall-normal, and spanwise direction. Uniform grids are used in the streamwise and spanwise directions, while a mapping function $y/h = \tanh(B\zeta)/\tanh(B)$, where $\zeta \in [-1, 1]$, $B = 2$, is employed for stretching the wall-normal grid. The specific heat ratio of the fluid is $\gamma = 1.4$. The reference values for the Sutherland equation used in the simulation are $S = 110.4$ K, $T_{\mathrm{ref}} = 293.15$ K, and $T_w = T_{\mathrm{ref}}$. The particle diameter is $d_p/h = 2.5 \times 10^{-3}$. The ratio of particle density to the fluid bulk density (ρ_b) is $\rho_p/\rho_b = 1000$. The bulk Reynolds number, the outer-scale particle Stokes number, the Prandtl number and the Mach number are $\mathrm{Re} = 3000$, $\mathrm{St} = 0.1, 1$, $\mathrm{Pr} = 0.72$, and $\mathrm{Ma} = 0.8,\ 1.5,$ and 2.0, respectively. The total number of the released particles is $N = 6 \times 10^5$, and therefore the particle volume fraction is $\Phi_V = 3.5 \times 10^{-6}$. The simulation cases for St = 1 and Ma = 0.8, 1.5, 2.0 are named R3M08S1, R3M15S1, and R3M20S1. In these cases, the viscous Stokes numbers St^+ are 10.8, 8.7, and 7.2. Similarly, the cases for St = 0.1 are named R3M08S01, R3M15S01, and R3M20S01, and the corresponding St^+ are 1.08, 0.87, and 0.72, respectively.

The time step for fluid and particle calculations is $\Delta t = 0.001h/U_b$. Each calculation runs for 5×10^6 time steps with a total computation time of $5000h/U_b$. The first 10^6 time steps are for the development of the single-phase turbulence. The well-established statistically quasisteady state of the two-phase turbulence is determined using the criterion that the change in the profiles of the mean turbulent velocity and the particle concentration to be less than 0.1%. The statistics are obtained by averaging the samples from $t^+ = \delta_\nu/u_\tau = 30\,000$ to 40 000, similar to the averaging methods used in Zhou *et al.* [61]. Details of the calculation parameters are also shown in Table I, where Δt^+ is the time step in the inner scale, Δx^+ and Δz^+ are the streamwise and spanwise grid spacing, and $\Delta y^+_{\max}$ and $\Delta y^+_{\min}$ are the maximum (channel center) and minimum (wall) grid spacing in the wall-normal direction, respectively. In this table, $\mathrm{Re}_\tau = \rho_w u_\tau h/\mu_w$.

TABLE I. Details of the calculation parameters.

Case	Re	Re_τ	Ma	St	St^+	Δt^+	Δx^+	Δz^+	Δy^+_{max}	Δy^+_{min}
R3M08S1	3000	198	0.8	1	10.8	0.013	7.3	4.9	6.4	0.47
R3M15S1	3000	219	1.5	1	8.7	0.015	8.1	5.4	7.1	0.52
R3M20S1	3000	240	2.0	1	7.2	0.019	8.8	5.9	7.8	0.56
R3M08S01	3000	198	0.8	0.1	1.08	0.013	7.3	4.9	6.4	0.47
R3M15S01	3000	219	1.5	0.1	0.87	0.015	8.1	5.4	7.1	0.52
R3M20S01	3000	240	2.0	0.1	0.72	0.019	8.8	5.9	7.8	0.56

To validate the code, we first compared the simulated results of unladen channel turbulence with previous DNSs at the same Re and Ma. Due to the compressibility, the traditional wall unit scaling cannot collapse the velocity profiles. Van Driest [62] proposed a well-known transformation $U^+_{VD}(y) = \int_0^{\bar{u}^+} \sqrt{\bar{\rho}/\bar{\rho}_w}\, d\bar{u}^+$ to account for the average density effects. Figure 1(a) shows the mean velocity profiles for Re = 3000 and Ma = 0.8, 1.5 in terms of the van Driest transformation. The results of Yao and Hussain [56] and the law of the wall (linear law and log law) are also illustrated. It is seen that the simulated results agree well with the transformed velocity profiles reported by Yao and Hussain [56], though both results show that the van Driest transformation overshoots the velocity profile in the log layer. Note that in spite of many other transformation at hand, they are not applied since this is beyond the scope of this study.

Then we check the simulated mean temperature. Walz [63] derived the compressible temperature-velocity relationship to conveniently predict the wall heat flux based on the compressible velocity transformations. The so-called Walz equation agrees well with DNS for boundary layer over adiabatic wall [64] but not that well for nonadiabatic cases [44]. The Walz equation was improved by introducing a general recovery factor r_g by Zhang *et al.* [65]. This improved temperature-velocity relationship, $\bar{T}/T_w = 1 + (T_{rg} - T_w)/T_w \bar{u}/U_c + (T_c - T_{rg})/T_w(\bar{u}/U_c)^2$ with $T_{rg} = T_c + r_g U_c^2/(2C_p)$ and $r_g = 2C_p(T_w - T_c)/U_c^2 - 2\,\mathrm{Pr}\,\bar{q}_w/(U_c^2\bar{\tau}_w)$, is adopted to rescale the simulated mean temperature distribution. Note that U_c and T_c are the centerline velocity and temperature of the channel, and $\bar{q}_w$ is the average heat flux at the wall. Figure 1(b) shows the mean temperature profiles as a function of $\bar{u}/U_c$ for $Re_b = 3000$ and Ma = 0.8, 1.5. The results of Yao and Hussain [56] and Zhang's equation are also shown. It is clear that the mean temperature-velocity relationships obtained agree well with the results of Yao and Hussain [56] and the Zhang's equation.

For the Reynolds stress $\tau_{ij} = \bar{\rho}R_{ij}$, where $R_{ij} = \widetilde{u_i u_j} - \widetilde{u}_i\widetilde{u}_j$, we show only the results $(\tau_{11}/\bar{\tau}_w, \tau_{22}/\bar{\tau}_w, \tau_{33}/\bar{\tau}_w)$ for Ma = 1.5 in Fig. 2(a). In this figure, the abscissa is the semilocal

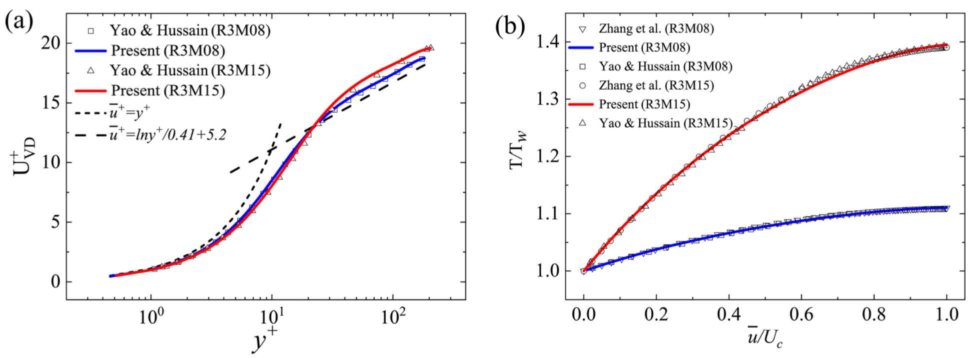

FIG. 1. (a) The average velocity profiles obtained from the van Driest transformation, linear law, log law, and the results of Yao and Hussain [56]. (b) The mean temperature-velocity relationship for the simulated data, compared with Zhang's equation and the results of Yao and Hussain [56].

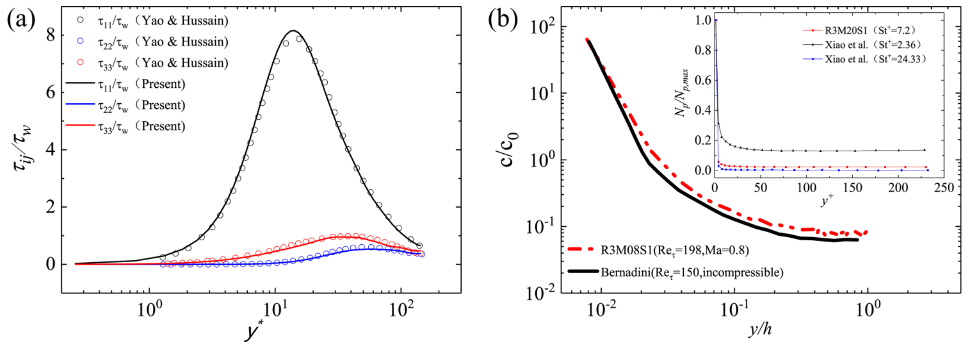

FIG. 2. (a) Semilocal transformation of Reynolds stress components as compared with the results of Yao and Hussain [56] for Ma = 1.5; (b) particle concentration profiles for R3M08S1 as compared with the results of Bernardini [18]. The inset in (b) shows the wall-normal distributions of particle number N_p normalized by the maximum particle number $N_{p,\max}$ for the simulation case of R3M20S1, together with the results of Xiao *et al.* [26] in a spatially developing compressible turbulent boundary layer at free-stream Mach number of 2.

wall-normal distance $y^* = y\mathrm{Re}_\tau^*$, where $\mathrm{Re}_\tau^* = \mathrm{Re}_\tau \sqrt{\bar{\rho}/\bar{\rho}_w}/(\bar{\mu}/\mu_w)$ is the semilocal friction Reynolds number. The Reynolds stresses are normalized by the semilocal friction velocity u_τ^* and expressed as R_{ij}/u_τ^{*2}, where $u_\tau^* = \sqrt{\bar{\tau}_w/\bar{\rho}}$. The results also show good agreement with those of Yao and Hussain [56].

Finally, we attempt to validate the particle solver. Since the compressible data available for comparison are few, we show in Fig. 2(b) only several selected particle profiles at similar parameters to cases R3M08S1 and R3M20S1. The particle concentration is normalized by the uniform distribution concentration c_0, and the particle number N_p is normalized by the maximum particle number $N_{p,\max}$ usually at the wall. It shows that the results of R3M08S1 (red dashed dot line, $\mathrm{Re}_\tau = 198$, Ma = 0.8) at the minimum Mach number are quite close to, though still higher than, the results of Bernardini [18] (black solid line, $\mathrm{Re}_\tau = 150$, incompressible) under similar particle inertia ($\mathrm{St}^+ \approx 10$). For the maximum Mach number (Ma = 2) case, the DNS result for $\mathrm{St}^+ \approx 7.2$ is compared with that of Xiao *et al.* [26] who reported the N_p profiles for two viscous Stokes numbers of $\mathrm{St}^+ = 2.36$ and 24.33. The inset in Fig. 2(b) indicates that the results of case R3M20S1 (Ma = 2, $\mathrm{St}^+ = 7.2$) are also between Xiao's two results, implying the rationality of the particle solver.

III. RESULTS AND DISCUSSIONS

A. The effects of Mach number on the turbophoresis

To investigate the Mach number effects on the particle segregation in compressible turbulent channel flow, we first visualize the particle distributions at different Mach numbers, taking St = 1 as an example. The instantaneous snapshots of particle positions in the range $-1.0 < y/h < 0$ and $0 < x/h < 3$ are shown in Fig. 3. The dots represent the particles that are colored by their dimensionless wall-normal velocity (v_p/U_b).

For all Mach numbers, there are more particles near the wall as compared to in the channel center, indicating a significant phenomenon of particle segregation. The magnitude of the particle wall-normal velocity is small near the wall. Therefore, particles are more difficult to move upwards, resulting in a longer accumulation time and higher particle concentration there. Interestingly, we observe more particles in the channel center at high Ma number. The less pronounced segregation phenomenon (particles are prone to accumulate near the wall) at higher Mach number means that the compressibility of fluid suppresses the particle segregation.

To better emphasize the accumulation process and clarify the effects of Mach number, we employ Shannon entropy [15] to quantify the degree of segregation. The Shannon entropy is calculated by

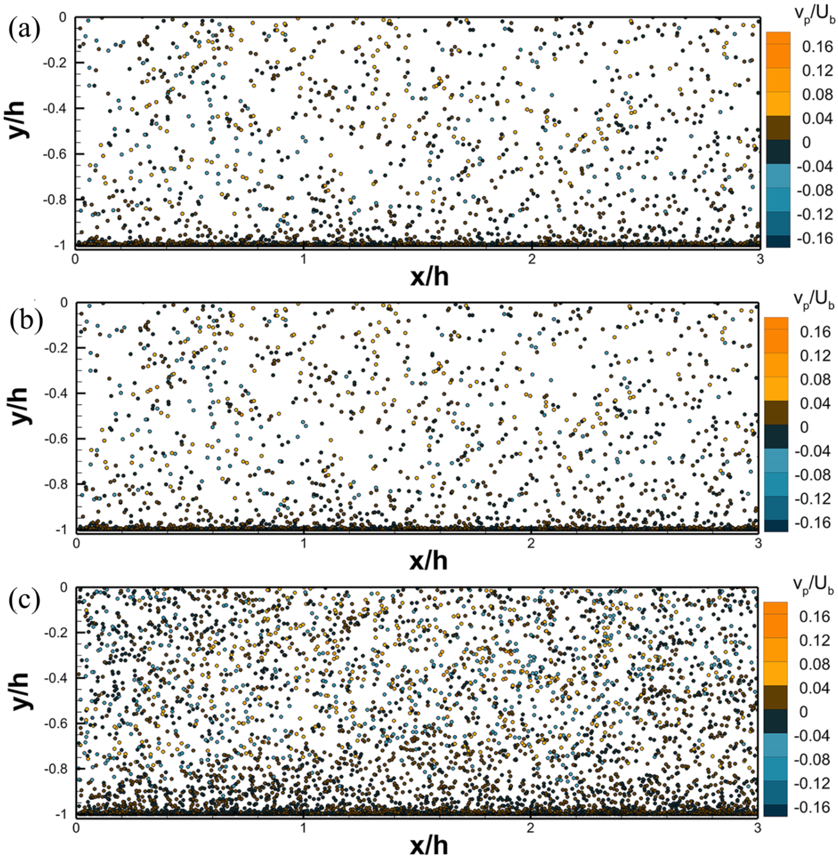

FIG. 3. Snapshots of particle distribution in the x-y plane. Particles with inertia of St = 1 are indicated by dots and colored by their wall-normal velocity. (a) Ma = 0.8, (b) Ma = 1.5, (c) Ma = 2.0.

$S = -\sum_{j=1}^{N_s} p_j \log p_j$, where N_s is the number of the equally spaced height bins of the simulation domain. The probability p_j is the ratio of the number of particles N_j in the jth height bin to the total number of particles N in the domain. The Shannon entropy is $S = 1$ if the particles are evenly distributed while $S = 0$ if all particles are deposited in the first off-wall bin. The simulation results of particle-laden incompressible channel turbulence by Picano *et al.* [15] indicated that as particles segregate, the Shannon entropy gradually decreases and finally reaches a statistically steady state after a certain period of time. This period of time depends on the flow Reynolds number and particle Stokes number.

Figure 4(a) shows the time evolution of Shannon entropy for different Stokes numbers at three Mach numbers. In all cases, the initial value of S is one, reflecting the initially uniform distribution of inertia particles in the turbulent channel flow. For St = 1, it can be clearly seen that the entropy slowly decreases as time goes by and gradually approaches a constant value at all Mach numbers. This behavior is consistent with previous observations in incompressible turbulence at similar Stokes number [18]. As discussed before, this intermediate Stokes number implies that the characteristic time of inertial particles matches the timescale of turbulent structures in the buffer layer of wall turbulence. Therefore, the turbulent regeneration cycle there controls the action of particles. Before being transported to the outer flow by the ejection-type events, particles will stay in the viscous layer for a long time [24], statistically resulting in the particle accumulation. However, the rate of decrease in the Shannon entropy parameter at lower Mach number is slower than that at

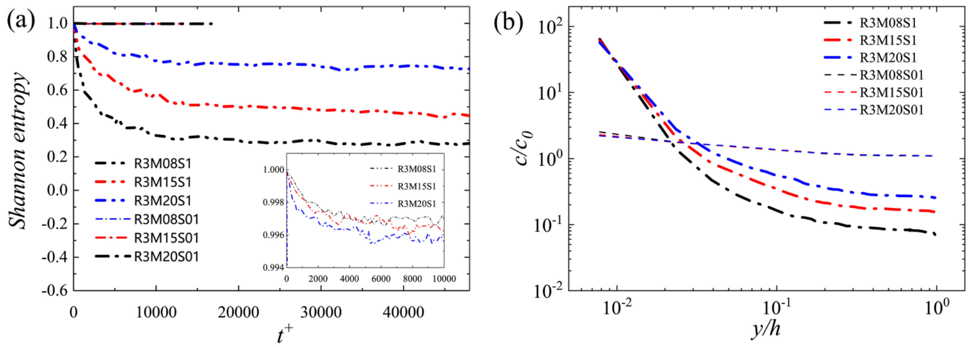

FIG. 4. (a) The evolution of Shannon entropy parameter. (b) Average particle concentration profiles. The inset in (a) shows an enlarged view of the Shannon entropy parameter around one from (a).

higher Mach number, and the S value at equilibrium is much higher. Obviously, the Mach-number dependence of particle accumulation also indicates varying near-wall turbulent structures associated with fluid compressibility, which will be discussed later. On the other hand, the accumulation of low-inertia particles (St $= 0.1$) in the wall region cannot be clearly detected though the inset in Fig. 4(a) does show an indistinct Mach-number dependence of the Shannon entropy evolution.

Figure 4(b) shows the particle concentration distributions as function of the outer-scale wall-normal height for different Stokes and Mach numbers. Note that the concentration c is scaled by the initially uniform distributed particle concentration c_0. For St $= 1$, c decreases monotonically and rapidly with the increase of y/h, and consequently, c at the center of the channel is several orders of magnitude lower than that near the wall. The effects of the Mach number on the mean concentration distribution of inertial particles can be easily observed, that is, higher Mach numbers result in higher particle concentrations in the channel center and vice versa. For St $= 0.1$, this phenomenon is not that obvious. We will try to discuss the Mach-number dependence of particle (St $= 1$) segregation in terms of the turbophoretic theory.

Caporaloni [22] pointed out that in incompressible turbulence, small and heavy particles tend to migrate from high- to low-intensity regions. The particle migration speed, known as the turbophoretic velocity, can be given by $v_{TF} = -\tau_p dv'^2/dy$, where v' is the vertical fluctuating velocity component of turbulence based on the Reynolds decomposition. The expression of the turbophoretic velocity indicates that v_{TF} is proportional to the gradient of turbulence intensity and the particle relaxation time, both of which may influence the particle migration. In the compressible turbulence, the particle relaxation time τ_p is no longer constant. Figure 5(a) shows the variation of τ_p with regard to y/h for all simulation cases. It is seen that τ_p decreases with the increase of y/h. The decrease is more rapid near the wall and at higher Mach number because in the near-wall region the temperature gradient increases as Mach numbers increase [66], and the particle relaxation time ($\tau_p = \rho_p d_p^2/18\mu$) is inversely proportional to the fluid dynamic viscosity and temperature according to Eq. (7). At the same time, it can be seen in Fig. 5(a) that τ_p in the channel center is smaller at high Mach numbers, since the temperature and dynamic viscosity is higher at high Mach numbers near the center of the channel [56].

The inset in Fig. 5(b) shows the profiles of the average wall-normal turbulence intensity v'^2, scaled by U_b^2. As the Mach number increases, v'^2 decreases in the near-wall region and slightly increases near the channel center. However, the gradients of v'^2 (not shown) in the near-wall region and the channel center both decrease as the Mach number increases. Similar results have be observed in the numerical simulations by Yao and Hussain [56].

The decreased τ_p on the one hand and the varying dv'^2/dy on the other determine the varying turbophoretic velocity with regard to the Mach number and the wall-normal height, as shown in Fig. 5(b). It is clear that the magnitude of v_{TF} increases apparently below the buffer layer and then

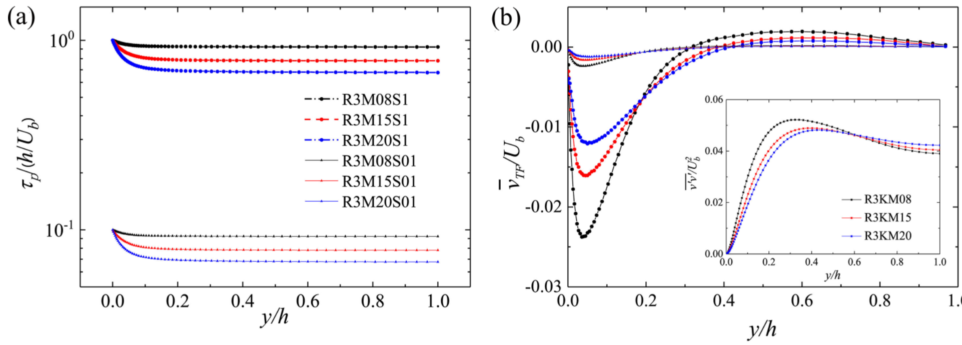

FIG. 5. (a) Particle relaxation time and (b) the turbophoretic velocity. The inset in (b) shows the turbulence intensity in the wall-normal direction.

decreases above. Actually, there always is a v_{TF} peak on each curve at about $y^+ \approx 9$ ($y/h \approx 0.04$). The negative v_{TF} will lead to strong particle net fluxes to the wall, which accounts for the near-wall accumulation of particles, and the relatively uniform particle distribution at high Mach number in the wall-normal direction can be attributed directly to the small $|v_{TF}|$. Far from the wall, $v_{TF} > 0$ suggests a turbophoretic drift of inertial particles towards the channel center. However, $|v_{TF}|$ is too small to generate a significant particle accumulation there.

The above discussion tells us that the compressibility manifests its influence on the particle distribution through affecting the turbophoretic drift. It is of interest to search for possible universality of concentration profiles for inertial particles in compressible turbulence. To this purpose, we start the analysis from the concentration diffusion equation provided by Reeks [23],

$$\frac{\partial c}{\partial t} = \frac{\partial}{\partial x_i}\left[\varepsilon_{ij}(\boldsymbol{x})\frac{\partial c}{\partial x_j} - \bar{u}_i(\boldsymbol{x})c + c\tau_p\frac{\partial \xi_{ij}(\boldsymbol{x})}{\partial x_j}\right] = \frac{\partial}{\partial x_i}[-j_i(\boldsymbol{x})]. \tag{10}$$

When the "turbulence-particle" system is fully developed, $\varepsilon_{ij} \to \overline{u_{p,i}x_{p,j}}$ and $\xi_{ij} \to \overline{u_{p,i}u_{p,j}}$ represent the particle diffusion coefficient and the mean square velocity tensor. $\bar{u}_i(\boldsymbol{x})$ is the ith-direction component of the mean fluid velocity at the particle position. The wall-normal component of the diffusion current $-j_i(\boldsymbol{x})$ is

$$-j_y(y) = \varepsilon_{yx}(y)\frac{\partial c}{\partial x} + \varepsilon_{yy}(y)\frac{\partial c}{\partial y} + \varepsilon_{yz}(y)\frac{\partial c}{\partial z} - \bar{v}(y)c + c\tau_p\frac{\partial \xi_{yx}(y)}{\partial x} + c\tau_p\frac{\partial \xi_{yy}(y)}{\partial y} + c\tau_p\frac{\partial \xi_{yz}(y)}{\partial z}. \tag{11}$$

In the homogeneous direction (streamwise and spanwise) of a turbulent channel flow, $\partial/\partial x = \partial/\partial z = 0$ and the mean wall-normal velocity $\bar{v}(y)$ is zero. Then the simple form of $j_y(y)$ is

$$j_y(y) = -\varepsilon_{yy}(y)\frac{\partial c}{\partial y} - c\tau_p\frac{\partial \xi_{yy}(y)}{\partial y}. \tag{12}$$

We recognize that the first term on the right side of the above expression is the diffusion term caused by the concentration gradient and the second term is consistent with the notion that given zero concentration gradients in any one direction, particles will migrate in an inhomogeneous flow from high- to low-turbulence intensities in the assumption that the mean square velocity of the particle equals that of the fluid [22,23]. Reeks [23] defined $-\tau_p\partial\xi_{ij}(y)/\partial y$ as the turbophoretic velocity. Its one-dimensional form, $-\tau_p\partial\xi_{yy}(y)/\partial y$, is identical to the one given by Caporaloni [22]. Therefore, the second term is essentially the turbophoresis transport. Rearranging the above expression, the wall-normal transport equation becomes

$$\frac{1}{\tau_p c}\frac{\partial c}{\partial y} = -\frac{\partial \xi_{yy}}{\varepsilon_{yy}\partial y} - \frac{j_y}{\tau_p\varepsilon_{yy}c}. \tag{13}$$

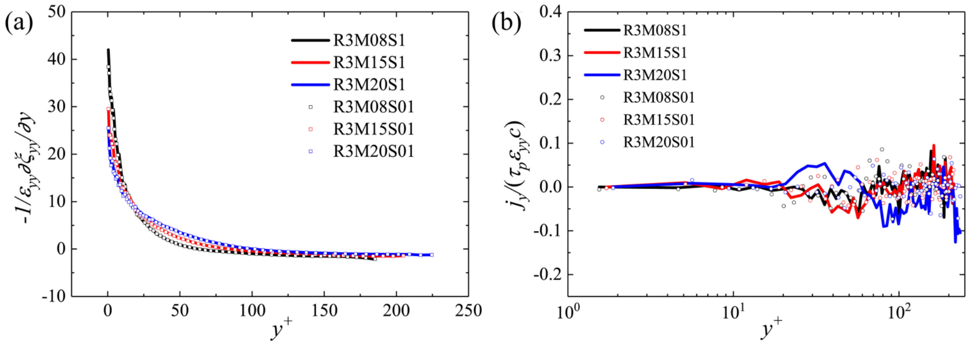

FIG. 6. (a) The first term on the right side of Eq. (14) $-1/\varepsilon_{yy}\partial\xi_{yy}/\partial$y as a function of y^+ and (b) the second term on the right side of Eq. (14) $j_y/\tau_p c\varepsilon_{yy}$.

Integrating Eq. (13) from the wall to arbitrary height y, then we obtain

$$\frac{1}{\tau_p}\int_{c_w}^{c}\frac{\delta c}{c}=\int_{y_w}^{y}-\frac{1}{\varepsilon_{yy}}\frac{\partial\xi_{yy}}{\partial y}\delta y-\int_{y_w}^{y}\frac{j_y}{\tau_p\varepsilon_{yy}c}\delta y, \tag{14}$$

where c_w is the particle concentration at the wall y_w. Figure 6(a) shows the first term on the right side of Eq. (14) as a function of the inner-scale wall-normal distance y^+. It can be observed that this term is relatively insensitive to the Mach number. The second term on the right side of Eq. (14) shown in Fig. 6(b) satisfies $j_y(y)=0$ near the wall (and is much smaller than $\partial\xi_{yy}/\partial y/\varepsilon_{yy}$ in magnitude), indicating a mean zero local diffusion current since the “turbulence-particle” system is fully developed and in a quasisteady state. Therefore, the term on the left side of Eq. (14) might be a reasonable combination that is independent of the Mach number. Then we get a particle concentration transformation as

$$\frac{1}{\tau_p}\ln\frac{c}{c_w}=\frac{1}{\tau_p}\int_{c_w}^{c}\frac{\delta c}{c}. \tag{15}$$

The dimensionless particle concentration (normalized by c_w) for all simulation cases and the incompressible reslut of Bernardini [18] based on the concentration transformation of Eq. (15) are shown in Fig. 7. Remarkably, the figure (as compared with the inset) highlights the collapse of the concentration profiles in the inner layer where both the compressibility and the inertia influence the most. For each inertia, the transformation is effective in the region where the particle relaxation time τ_p rapidly changes [see Fig. 5(a)]. For different Mach number and incompressible situation, the introduction of the reciprocal particle relaxation time helps to collapse substantially the curves with different particle inertia, probably supporting the universality of exponential distribution of inertial particle concentration (all curves collapse in log plot). We emphasize that the turbulent Reynolds number is in a small range of $198<\mathrm{Re}_\tau<240$ for the studied compressible wall turbulence, which might be one of the important reason for the clear inner-region scaling law.

B. The effect of Mach number on the preferential distribution

The preferential distribution of inertial particles in incompressible wall turbulence and the underlying mechanisms related to turbulent structures have been well documented [16,24,37]. Since the turbulence structure could be modified by the compressibility [43,67]. The Mach number dependence of the preferential distribution of the particles in compressible turbulence is expected. The discussions are mainly based on the simulation results for $\mathrm{St}=1$, while those for $\mathrm{St}=0.1$ will be mentioned when necessary.

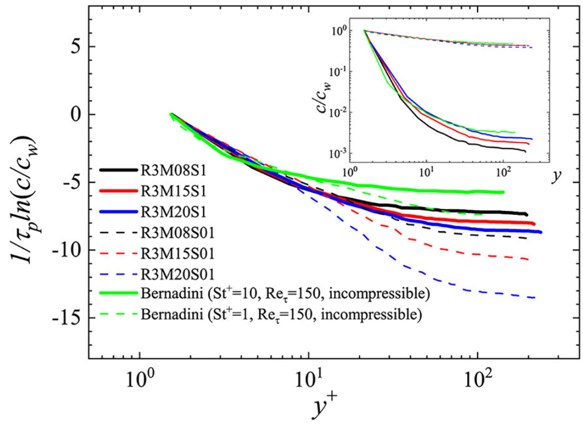

FIG. 7. Concentration profiles using reciprocal particle relaxation time weighting transformation $1/\tau_p \ln(c/c_w)$. The inset is the particle concentration normalized by the wall particle concentration c/c_w.

Figure 8 shows the instantaneous particle distribution in the inner region ($y^+ \approx 15$) and the outer region ($75 < y^+ < 125$). The black dots represent particles and colors represent the values of the dimensionless streamwise fluctuation velocity u'/U_b at $y^+ \approx 15$ and $y^+ \approx 100$, respectively. For a better presentation of spatial distribution, particles are enlarged. Note that we present the particles in the range of $75 < y^+ < 125$ because the number of particles in the outer region is few, as shown in Fig. 4(b).

From Figs. 8(a), 8(c), and 8(e), it is clear that the particles tend to cluster in the near-wall low-fluid-speed regions. This is consistent with previous studies on incompressible particle-laden flow

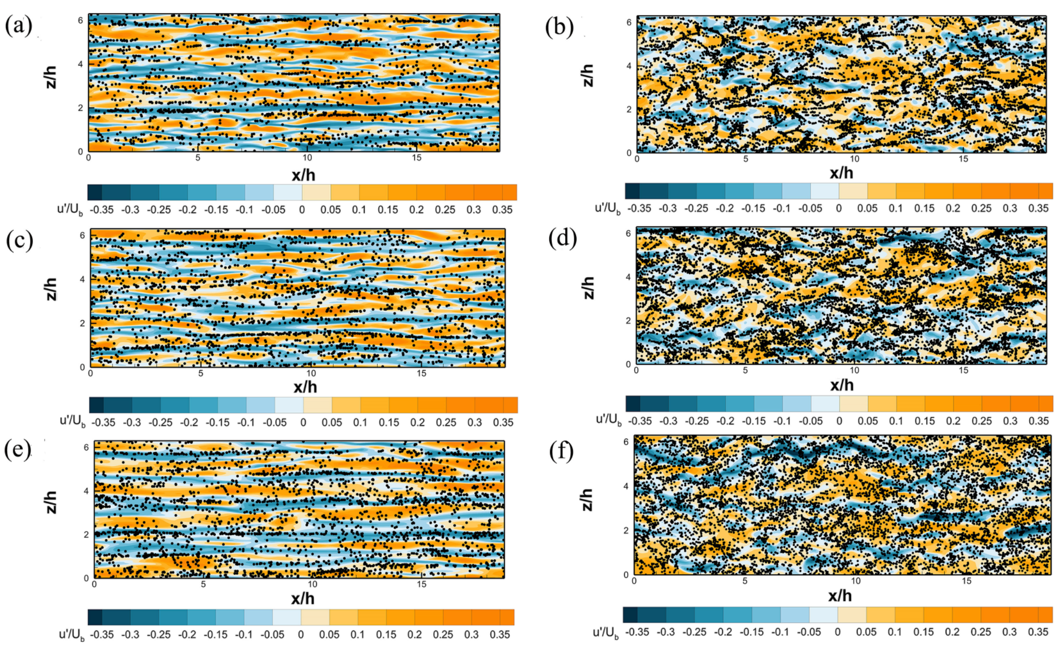

FIG. 8. Particle distribution at $y^+ \approx 15$ for (a) Ma = 0.8, (c) Ma = 1.5, and (e) Ma = 2.0 and in the region of $75 < y^+ < 125$ for (b) Ma = 0.8, (d) Ma = 1.5, and (f) Ma = 2.0. The black dots represent particles, and colors represent the values of the dimensionless streamwise fluctuation velocity u'/U_b.

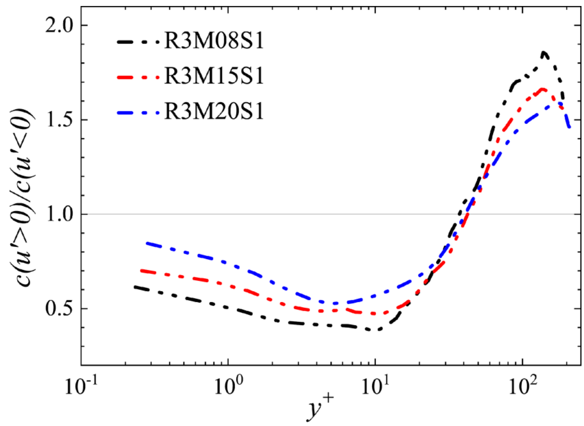

FIG. 9. Ratio of particle concentration in high-speed regions ($u' > 0$) to that in low-speed regions ($u' < 0$).

[24]. However, as the Mach number increases, the number of particles in high-fluid-speed regions increases and the preferential distribution phenomenon becomes less pronounced. Figures 8(b), 8(d), and 8(f) show that in the outer region particles tend to distribute in high-speed regions, consistent with the results of Wang and Richter [37] for incompressible open-channel turbulence and Xiao *et al.* [26] for compressible turbulent boundary layers. Analogously, the tendency is less clear at higher Mach number. The preferential distribution is straightforwardly quantified by counting the particle positioned in high-fluid-speed ($u' > 0$) and low-fluid-speed ($u' < 0$) regions, respectively. The ratios of the particle concentration $c(u' > 0)$, corresponding to these particle counts, to $c(u' < 0)$ are shown in Fig. 9. Here there is a clear monotonic trend of the ratio with the Mach number and a nonmonotonic trend with y^+. The latter has already been observed in incompressible turbulence. However, the Mach number dependence has never been reported before to the best of our knowledge.

As the Mach number increases, in the near-wall region, the particle preferential accumulation in the low-speed regions weakens. The Mach number dependence of the particle preferential distribution in the near-wall region can be first explained by the changes in near-wall turbulent events. We show in Fig. 10(a) the conditionally sampled events $\overline{u'v'_q}/U_b^2$ that particles reside in, where the subscript "q" represents a specific quadrant, for case R3M08S1. The events corresponding to each quadrants are Q1($u' > 0$, $v' > 0$), Q2($u' < 0$, $v' > 0$), Q3($u' < 0$, $v' < 0$), and Q4($u' > 0$, $v' < 0$).

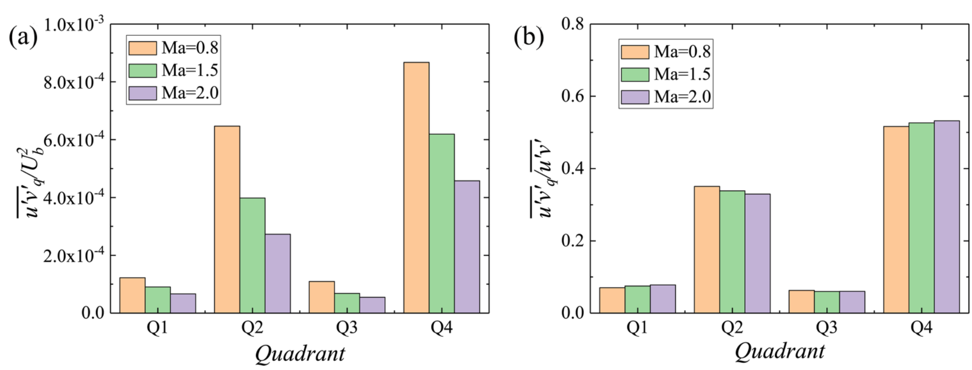

FIG. 10. (a) Fluid event intensities $\overline{u'v'_q}/U_b^2$ in each quadrant and (b) the quadrant contributions to the Reynolds shear stress $\overline{u'v'_\mathrm{q}}/\overline{u'v'}$ at $y^+ \approx 15$.

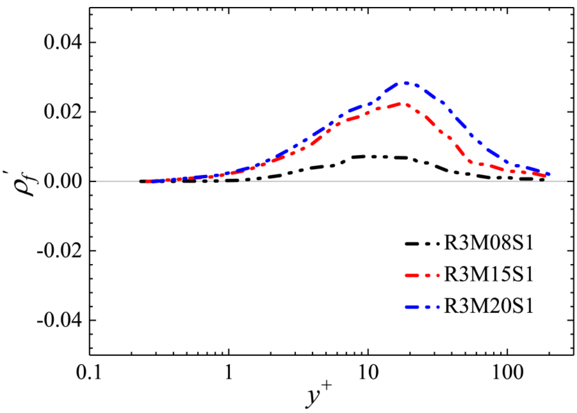

FIG. 11. Wall-normal profiles of the fluid fluctuation density at the particle positions ρ_f'.

The quadrant contributions to the Reynolds shear stress are presented in Fig. 10(b). Figure 10 indicates that the events are all weakened with the increase of Ma, though there is little change in the proportion of events. Note that particles are mainly distributed in Q2 (sweep) and Q4 (ejection) events due to the effect of the quasistreamwise vortex. The reduced event intensities, on one hand, cause difficulty for particles transporting in the wall-normal direction (weak segregation as discussed above) and, on the other hand, homogenize the particle distribution in horizontal plane (less pronounced preferential concentration phenomenon). The latter will be further discussed later in terms of the conditional hairpin vortex.

As the Mach number increases, in the outer region, the particle preferential accumulation in the high-speed regions weakens. In a study on incompressible particle-laden flow, Wang and Richter [37] observed that the most significant preferential accumulation occurred when $\mathrm{St}_{\mathrm{out}} = 6.0$ (defined as $\mathrm{St}_{\mathrm{out}} = \tau_p/\tau_f^{\mathrm{out}}$), and accumulation weakens as $\mathrm{St}_{\mathrm{out}}$ continues to decrease. For the cases presented in this paper, the $\mathrm{St}_{\mathrm{out}}$ of particles gradually decreases as the Mach number increases. For example, when $\mathrm{St} = 1$ and the Mach number varies from 0.8 to 2.0, $\mathrm{St}_{\mathrm{out}}$ decreases from 0.92 to 0.67 at the center of the channel, as illustrated in Fig. 5(a). The $\mathrm{St}_{\mathrm{out}}$ effects are consistent with the findings of Wang and Richter [37], and in this paper, $\mathrm{St}_{\mathrm{out}}$ effects are attributed to the reduction in τ_p as the Mach number increases. Nevertheless, higher Mach numbers suppress the phenomenon of particle preferential accumulation in the high-speed regions of the outer region.

Figure 11 shows that the wall-normal profiles of the fluid fluctuation density ρ_f' observed at particle positions are greater than zero at all Mach numbers throughout the channel. This implies that particles have a tendency to accumulate in high-density regions in both the inner and outer region. In the outer region of incompressible turbulent flow, particles tend to accumulate preferentially in low-vorticity regions outside the vortex due to the centrifugal effects [12]. Whereas in compressible turbulent flow, these regions correspond to the compressed high-density regions outside the vortex. Consequently, particles exhibit a tendency to accumulate in high-density regions [68]. In the inner region, for $\mathrm{Ma} = 0.8$, 1.5, and 2.5, the conditionally averaged fluid density fluctuations ρ_f' reach their peaks at $y^+ \approx 13$, 18, and 20, respectively, indicating that preferential accumulation of particles is most evident there. As the Mach number increases, the peak of ρ_f' gradually increases, because this is due to higher Mach number and leads to an augmentation of fluid density fluctuation in the inner region [43]. Note that the high-density distribution of particles in the inner region in this study differs from the results of Xiao *et al.* [26], in which a low-density-region distribution of particles was reported. This difference should be attributed to the wall temperature effects. The adiabatic wall temperature employed in Xiao's simulation corresponds to a clear correlation between low-speed and low-density regions [26], whereas a cold wall in this study will result in an apparent correlation between low-speed and high-density regions [69] in the inner region.

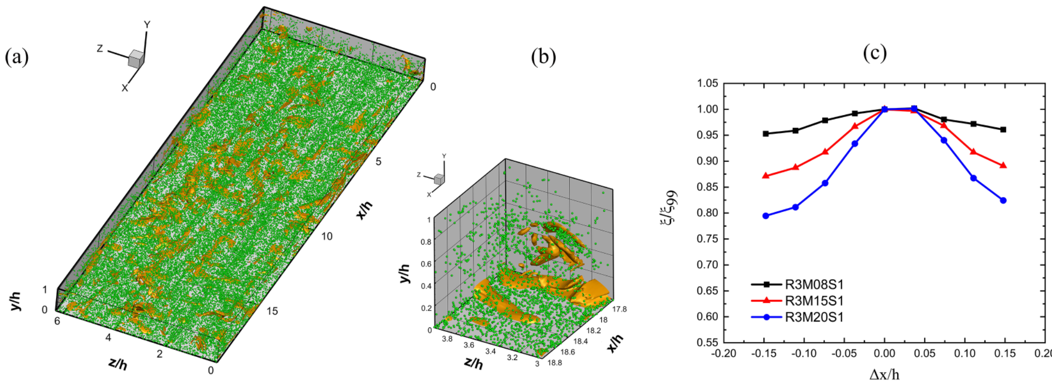

FIG. 12. (a) Instantaneous isosurfaces of velocity divergence $\theta = -\theta'_{rms}|_w$ (orange) for case R3M20S1. $\theta'_{rms}|_w$ is the root-mean square of velocity divergence fluctuation at the wall. The green spheres represent particles. (b) The enlarged view of a typical compression structure and nearby particle distribution. (c) Particle number density near the extreme compression events for cases R3M20S1, R3M08S1, and R3M15S1 (St = 1) along the streamwise direction, normalized by ξ_{99} (the conditional average of particle number density at extreme compression events $E = [\theta < 0, \text{and } |\theta| > 0.99|\theta_{\min}|]$).

Apart from the turbulent velocity and density fluctuation, the particle distribution is also relevant to the local compressibility of the fluid. Figure 12(a) shows the instantaneous isosurfaces of velocity divergence($\theta = \nabla \cdot u$, $\theta < 0$ indicates that the fluid is being compressed, while for $\theta > 0$, the fluid is expanding in those regions) for Ma = 2.0. The isosurfaces of velocity divergence are colored in orange, whereas the green points represent particles. The reference value of the isosurface is set to be the negative root mean square of velocity divergence fluctuation at the wall, denoted as $\theta'_{rms}|_w$. This visualization method was also employed by Yu *et al.* [70]. Since the turbulent Mach numbers are not high enough, we just call the identified the isosurfaces as compression structures, instead of shocklets. It can be seen that the compression structures are randomly distributed in the flow field, mainly in the near-wall region.

To look at the particle distribution more clearly, a close-up view is provided in Fig. 12(b). It can be observed that particles tend to accumulate near the compression structures. For further discussions, we calculate the conditionally averaged particle number. The extreme compression events $E(\theta)$ are chosen as $E = [\theta < 0, \text{and } |\theta| > 0.99|\theta_{\min}|]$. $\xi_{99} =< \xi|E >$ represents the conditional average of particle number density at extreme compression events. $\xi(\Delta x)$ or $\xi(\Delta z)$ represents conditional average of particle number density at distance Δx or Δz away from extreme compression events.

Figure 12(c) shows the particle number density near the extreme compression events. It can be seen that near the events, particle number density decreases with increasing streamwise distance, which indicates that particles tend to accumulate near the events. This phenomenon becomes more pronounced with increasing Mach number. However, a higher particle number density is observed for $\Delta x > 0$. This is because that when the particles pass through a compression structure, they will decelerate and accumulate downstream, leading to a higher particle number density there. This downstream accumulation phenomenon was also observed by Yang *et al.* [9], though the flow pattern is different and M_t in this study is also much smaller.

As shown in the previous Fig. 12, particles tend to accumulate near the extreme compression events. Furthermore, we give the probability density functions (PDFs) of dilatation (velocity divergence) at particle positions in both the inner and outer regions of wall turbulence to provide a global perspective. In Fig. 13(a) we present the PDFs of dilatation conditionally sampled at particle positions in the outer region of $y^+ \approx 50$. The results show that the average dilatations for Ma = 0.8, 1.5, and 2.0 are -7.8×10^{-4}, -1.1×10^{-3}, and -3.5×10^{-3}, respectively. The negative

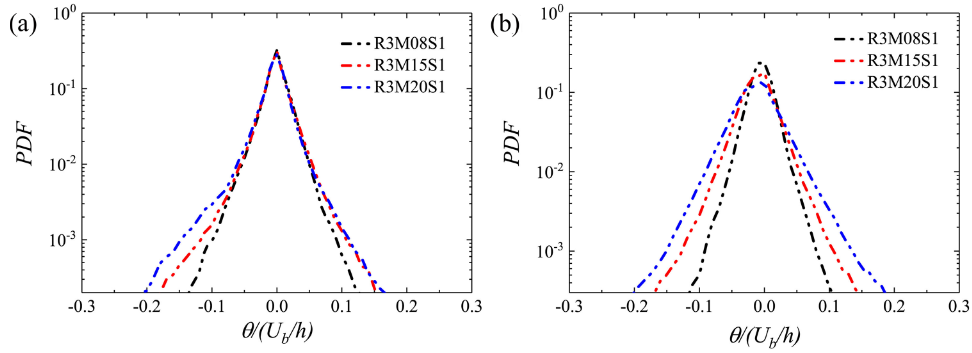

FIG. 13. Probability density functions (PDFs) of dilatation θ at particle positions in (a) the outer region $y^+ \approx 50$ and (b) the inner region $y^+ \approx 15$.

dilatation suggests that the fluid at the location where the particles are present exhibits a more pronounced average compressibility, similar to the previous results of Yang *et al.* [9]. In the inner region, however, things will be more complex. Figure 13(b) shows the PDFs of the dilatation at the particle positions at $y^+ \approx 15$. For the cases with Ma $= 0.8$, 1.5, and 2.0, the average dilatations are -5.0×10^{-3}, -9.7×10^{-3}, and -1.1×10^{-2}, respectively, indicating that particles are also accumulated in the compressed regions. Meanwhile, the average of the conditional dilatations in the inner region are larger than those in the outer region due to the stronger compressibility of the fluid itself in the inner region [56]. Accordingly, we propose a combination mechanism between the turbulent velocity structure and the compressibility for particle preferential distribution.

In Fig. 14 we show the joint distribution between the conditional streamwise velocity fluctuation u' and the dilatation θ at particle position in the inner region ($y^+ \approx 15$). The proportions of particles in the four quadrants, named O1($u' > 0, \theta > 0$), O2($u' < 0, \theta > 0$), O3($u' < 0, \theta < 0$), and O4($u' > 0, \theta < 0$), are also presented in the figures. First, the joint distribution is skewed with the minimum proportion being in O1 quadrant, which indicates that particles are least likely detected in high-fluid-velocity and expansion regions. That in O4 quadrant takes the second least place. The particles distributed in the second quadrant are always the most abundant. The sum of particle number in the second and third quadrants (low-fluid-velocity regions) are 68.5% for Ma $= 0.8$, 65.5% for Ma $= 1.5$, and 63.8% for Ma $= 2.0$. The cluster of particles in the low-fluid-speed regions and the reduced preferential distribution with Mach number coincide with what observed in Fig. 9(a). On the other hand, the sum of the O3 and O4 distribution is always greater than 50%. Second, it is notable that as the Mach number increases (Ma $= 0.8 \rightarrow 1.5 \rightarrow 2.0$), the particles in O1 quadrant and O3 quadrant decrease (O1: 9.7% $\rightarrow$ 8.6% $\rightarrow$ 8.2%, O3: 34.6% $\rightarrow$ 30.3% $\rightarrow$ 26.6%), while those in O2 quadrant and O4 quadrant increase (O2: 33.9% $\rightarrow$ 35.2% $\rightarrow$ 37.2%, O4: 21.8% $\rightarrow$ 25.9% $\rightarrow$ 28.0%). It seems that the enhancement of the local expansion is accompanied by the particle distribution in the high-fluid-speed regions (O2), while the enhancement of the local compression suppresses the particle distribution in the low-fluid-speed regions (O3). Similar to the overall compressibility effects in Fig. 9, local compressibility inhibits the intensity of local ejection events, thereby suppressing the preferential accumulation of particles in the low-speed regions. Finally, as the Mach number increases, since the percentage decrease in particle distribution in the O3 regions is greater than the percentage increase in the O2 regions, the local compressibility effects (including expansion and compression) overall weaken the preferential particle accumulation in low-speed regions. Additionally, the transport of particles is driven by near-wall ejection events. When particles pass through a compression structure, they will decelerate, thereby weakening the particle transport and the preferential accumulation in low-speed regions.

The nonuniform distribution of particles in the horizontal plane leads to the particle streaks and the organized particle structures, as illustrated in Fig. 8. We calculated the two-point correlation

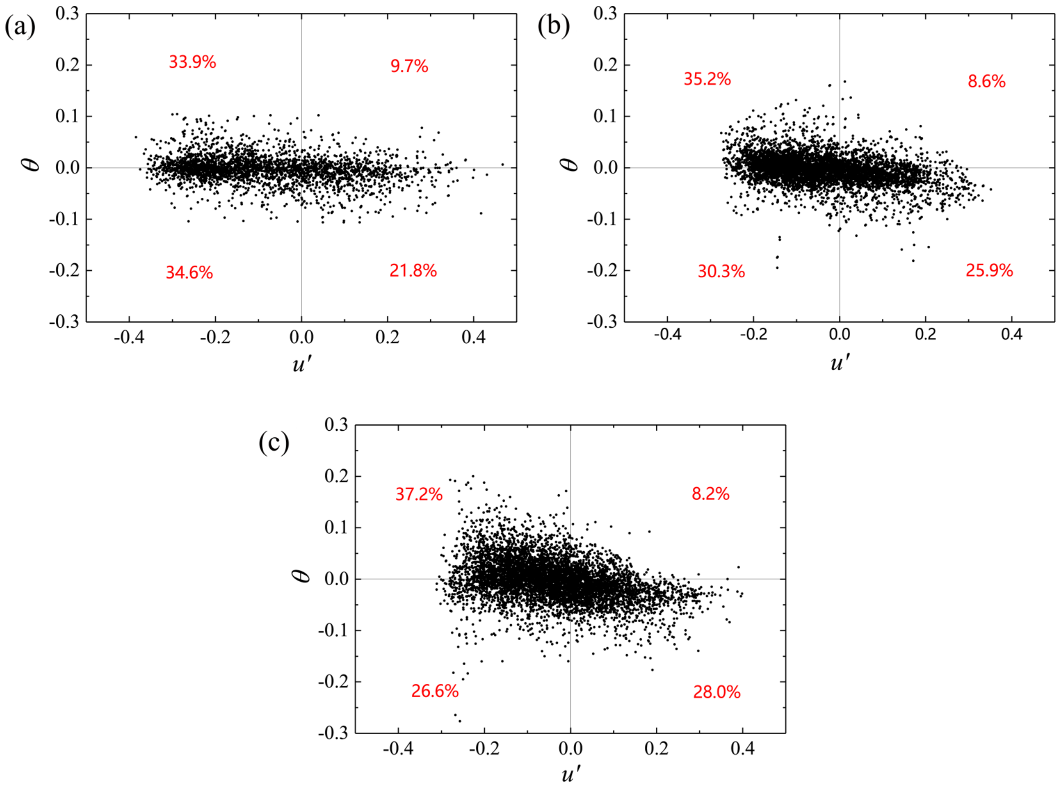

FIG. 14. Joint distribution between the conditional streamwise velocity fluctuation u' and the dilatation θ at particle locations in the inner region ($y^+ \approx 15$). (a) Ma = 0.8, (b) Ma = 1.5, (c) Ma = 2.0 for St = 1.

coefficient $R_{c'c'}$ of particle concentration to quantify the scales of particle structures. The autocorrelation coefficients in the streamwise direction is defined as

$$R_{c'c'}(\Delta z) = \langle c'(x, y_{\mathrm{ref}}, z, t)c'(x, y_{\mathrm{ref}}, z + \Delta z, t)\rangle / \langle c'(x, y_{\mathrm{ref}}, z, t)c'(x, y_{\mathrm{ref}}, z, t)\rangle, \tag{16}$$

and that in the spanwise direction is

$$R_{c'c'}(\Delta x) = \langle c'(x, y_{\mathrm{ref}}, z, t)c'(x + \Delta x, y_{\mathrm{ref}}, z, t)\rangle / \langle c'(x, y_{\mathrm{ref}}, z, t)c'(x, y_{\mathrm{ref}}, z, t)\rangle, \tag{17}$$

where $c' = c - \bar{c}$, y_{ref} is the reference height. The results are shown in Fig. 15. Again, $R_{c'c'}$ in the outer region is calculated in terms of the particles distributed within the height range of $75 < y^+_{\mathrm{ref}} < 125$ since the number of particles in the grid space at a specific height there is not enough to achieve a smooth statistical curve.

It is seen from Fig. 15(a) that the first local minimum values of the spanwise two-point correlations occur in general at $\Delta z^+ \approx 50$–60, and this implies an average spanwise spacing of approximately 120 in viscous units, which is similar to the numerical results of Sardina *et al.* [35] in incompressible turbulence. However, the average spanwise spacing of particle streaks gradually increases with the increase of the Mach number. It is approximately 106 viscous units for Ma = 0.8, 118 viscous units for Ma = 1.5, and 129 viscous units for Ma = 2.0. Figure 15(b) shows the streamwise two-point correlation of particle concentration at the height of $y^+_{\mathrm{ref}} \approx 15$. Although the computational domain is not sufficient long for $R_{c'c'}$ decaying to zero, it can be observed that $R_{c'c'}$ increases with the Mach number.

Actually, the contours of the instantaneous streamwise fluctuating velocity in Fig. 8 become less meandering at high Mach number, suggesting a widened and elongated correlation region.

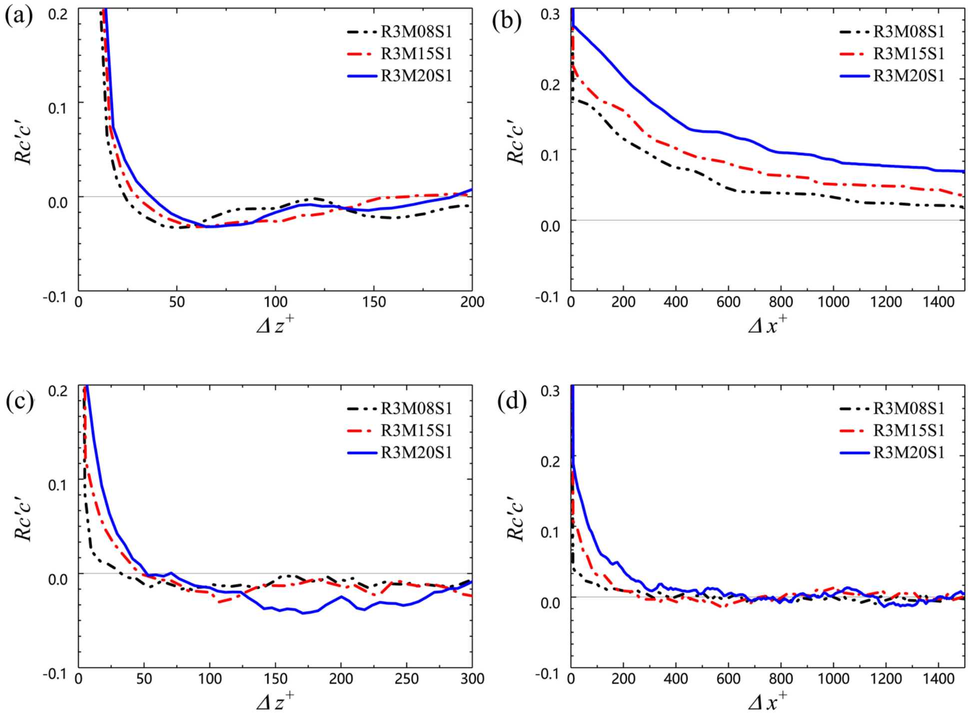

FIG. 15. Two-point correlation of particle concentration in (a) the spanwise direction and (b) streamwise direction at a reference height of $y^+_{\mathrm{ref}} \approx 15$. (c), (d) $R_{c'c'}$ for particles within the height range of $75 < y^+_{\mathrm{ref}} < 125$. Lines: dash–dot-dotted, Ma = 0.8; dash–dotted, Ma = 1.5; solid, Ma = 2.0.

Therefore, naturally, the particle streaks become larger at high Mach number, due to the one-way coupling and the moderate inertia.

Figures 15(c) and 15(d) show the streamwise and spanwise two-point correlations of particle concentration in the outer region, $75 < y^+_{\mathrm{ref}} < 125$. Although the correlation coefficients exhibit significant fluctuations in their decay stages with respect to Δz^+ and Δx^+, it can still be observed from the figures that the average streamwise spacing in the outer region is greater than that in the inner region. Additionally, the average streamwise spacing and streamwise scale of particle structures in the outer region tend to increase with increasing Mach number, similar to the trends observed in the inner region.

From the above discussions and numerous previous studies, it has been well established that ejection and sweep events account for the particle preferential distribution. On average, individual hairpin vortices serve as the near-wall coherent structures responsible for ejection and sweep, contributing significantly to the mass and momentum transport near the wall. Hairpin vortices grow and combine to form packets of hairpin vortices in the logarithmic region, i.e., large-scale motions [71]. To explain the variation in the scales of particle structure with Mach number, the linear stochastic estimation (LSE) method is employed to extract conditional hairpin vortex structures.

One can refer to [72] for the LSE theory. This method has been widely used to study the characteristics of particles around the vortices in two-phase wall turbulence [33,73]. Here we provide just a brief description of LSE. Given the event $E(\chi^*, t)$ at event location χ^*, the conditional average of a fluctuating quantity ψ at location χ is denoted $\langle \psi | E \rangle$. E represents the ejection events. LSE approximates the linearly estimated field $\hat{\psi}(\chi)$ as $\hat{\psi}_i(\chi) = L_{ij}(\chi, \chi^*)E_j(\chi^*)$, where L_{ij} provides the best linear approximation of the conditional mean $\langle \psi | E \rangle$ using the least squares method. The conditional field $\hat{\psi}(\chi)$ that we are currently interested in includes the turbulent velocity

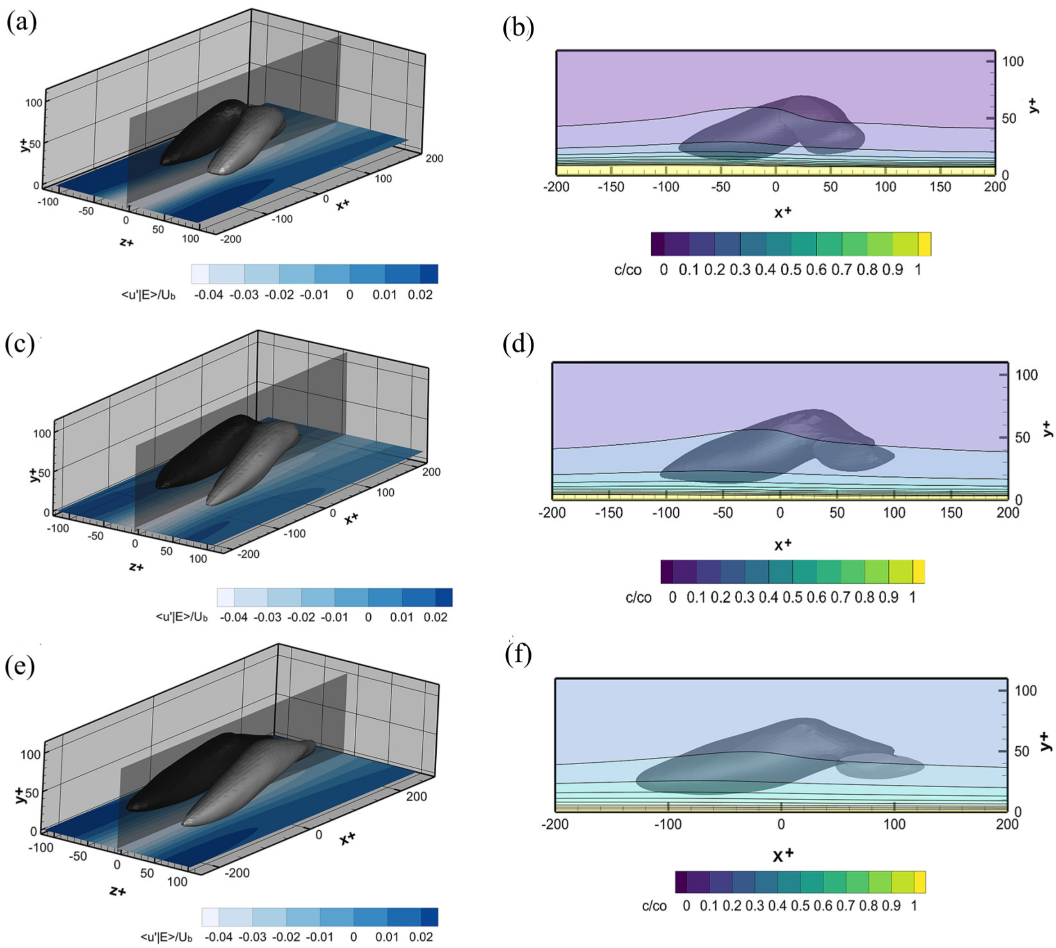

FIG. 16. (a) Conditional structures $E = [u'_m, v'_m, 0]$ obtained using the LSE method and visualized using the $|\lambda_{ci}|/(U_b/h)$ and (b) conditional particle fluctuating concentration $\langle c'|E\rangle/c_0$ on the vertical slice at $z^+ = 0$ for Ma $= 0.8$ and St $= 1$. The middle (c), (d) and bottom (e), (f) rows correspond to those for Ma $= 1.5$ and Ma $= 2.0$, respectively. The horizontal slices of conditional streamwise velocity fluctuations $\langle u'|E\rangle/U_b$ in the left column is positioned at $y^+ = 8$.

fluctuations and the particle concentration field, namely, $\hat{\psi}(\chi) = [\hat{u}', \hat{v}', \hat{w}', \hat{c}']$. The ejection events $E(\chi^*, t)$ is chosen as $E = [u'_m, v'_m, 0]$. The selection of u'_m and v'_m is based on maximizing the product of their joint probability density $P(u'_m, v'_m)$.

Figures 16(a), 16(c), and 16(e) show the variation of the conditional structures obtained using linear stochastic estimation as the Mach numbers increases, with the event location being at $y^+ \approx 50$. The gray structures represent the isosurface where the squared swirling strength $|\lambda_{ci}|^2$ is equal to 20% of the maximum value of each simulation case. The definition of swirling strength λ_{ci} (the imaginary part of the complex eigenvalue of the fluid velocity gradient tensor $\nabla\mathbf{u}$) can be found in the article of Zhou *et al.* [74]. The horizontal planes in the left column located at $y^+ = 8$ show slices of the conditional streamwise velocity fluctuations $\langle u'|E\rangle/U_b$. The structures of vortices are similar in shape for all Mach numbers. The length of vortex legs increases and the vortex structure becomes flatter as the Mach number increases. This is consistent with the numerical results of Liang and Li [67]. In compressible turbulence, compressibility effects lead to obvious increase of pressure work and dilatational dissipation according to Yu *et al.* [70], and part of turbulent kinetic energy

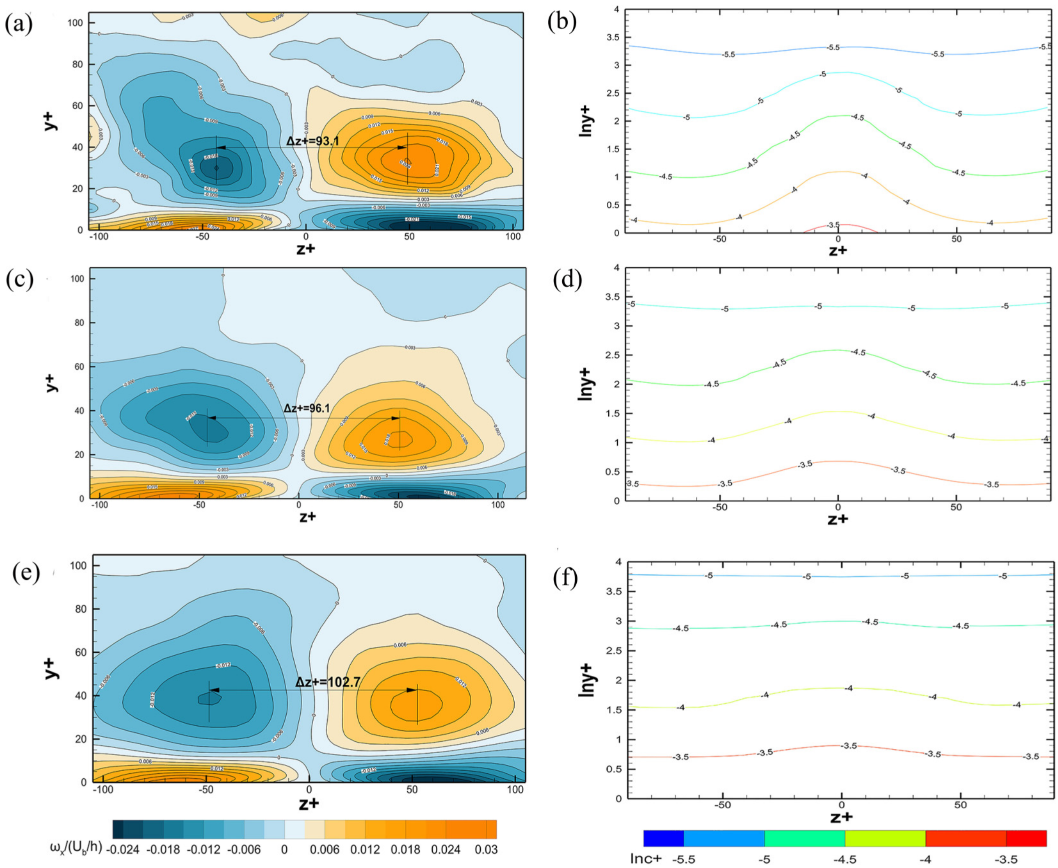

FIG. 17. Conditional average streamwise vorticity obtained using LSE for different Mach numbers: (a) Ma = 0.8, (c) Ma = 1.5, and (e) Ma = 2.0, and the contours of conditional average particle concentration (b) Ma = 0.8, (d) Ma = 1.5, and (f) Ma = 2.0.

is absorbed and the turbulence intensity is suppressed [48], thereby the near-wall velocity streak structures become flatter.

Figures 16(b), 16(d), and 16(f) show the conditional structures and contour lines of particle concentration in the vertical slices at $z^+ = 0$. In the low-speed ejection regions between the counter-rotating vortex legs, but upstream of the conditional eddy, the elevated high particle concentrations can be observed. This higher concentration than the horizontal average further indicates the influence of the ejection of the Q2-based conditional hairpin vortex on preferential accumulation, corresponding also to the nonuniform distribution of particles in the horizontal plane. As the Mach number increases, however, the contour lines of particle concentration become flatter and the upwelling angle of high-concentration region decreases, confirming the reduced nonuniformity of particle distribution and the longer streamwise scale of particle structures.

Figure 17 shows the contours for the conditional average of streamwise vorticity ω_x and particle concentretion on the y-z plane for different Mach numbers, where $\omega_x = \partial w/\partial y - \partial v/\partial z$, and v and w represent the wall-normal and spanwise turbulent velocities, respectively. From Figs. 17(a), 17(c), and 17(e), it can be observed that there is a pair of counter-rotating quasistreamwise vortices on both sides of the symmetric Q2 event point (at $z^+ = 0$, $y^+ \approx 50$), a clockwise vortex ($z^+ \approx 50$) and an anticlockwise one ($z^+ \approx -50$). The combined effect of these two vortices near $z^+ \approx 0$ corresponds to the ejection events. As the Mach number increases (Ma = 0.8 → 1.5 → 2.0), the maximum value of ω_x gradually decreases ($\omega_{x,\max} = 0.025 \rightarrow 0.020 \rightarrow 0.017$), which leads to the weakening of the ejection events. At the same time, the spacing between the counter-rotating vortices (i.e., the distance between the centers of two vortices) Δz^+ increases as the Mach number increases ($\Delta z^+ = 93.1 \rightarrow 96.1 \rightarrow 102.7$). This implies an increase in the streamwise scale of fluid streaks.

The particles are transported upward through these two counter-rotating vortices in the ejection events, ultimately accumulate near $z^+ \approx 0$ (the low-speed region below the symmetric Q2 event point). The conditionally averaged particle concentration distributions calculated based on the symmetric Q2 event locations are shown in Figs. 17(b), 17(d), and 17(f), in which the wall-normal axis is the logarithmic scale $\ln y^+$. It can be seen that between the vortices ($z^+ \approx 0$), the particle concentration contours bulge toward the outer region, indicating particle accumulate in these regions and the formation of particle streaks. As the Mach number increases, the phenomenon of the contours bulging toward the outer region decreases, indicating a reduction in particle accumulation.

IV. SUMMARY

The effects of Mach number on turbophoresis and the preferential accumulation of inertial particles in compressible channel turbulence are investigated. Direct numerical simulations of two-phase flow are conducted in the Eulerian-Lagrangian framework at a bulk Reynolds number $\mathrm{Re}_b = 3000$, particle Stokes numbers $\mathrm{St} = 0.1$ and 1, and Mach numbers $\mathrm{Ma} = 0.8$, 1.5, and 2.0.

As the Mach number increases, the turbophoresis-induced particle segregation is suppressed. The particle concentration near the center of the channel increases, while that in the near-wall region decreases. This can be attributed to the reduced particle relaxation time, the varying wall-normal turbulence intensity, and consequently the decreased turbophoresis velocity at high Mach numbers. By considering the Reeks' concentration diffusion equation, we propose a particle relaxation time weighting transformation to collapse particle concentration. The transformed particle concentration profiles at different Mach numbers and in the incompressible situation collapse in the inner scales and in the inner region.

In compressible channel turbulence, particles in the inner region tend to preferentially cluster in the low-fluid-speed regions, while those in the outer region tend to distribute in the high-fluid-speed regions, which is consistent that in incompressible wall turbulence. However, this preferential concentration phenomenon is less pronounced with increasing Mach number due to the modified turbulent structures. Quadrant analysis of the turbulent velocity conditionally sampled at particle position shows that although the proportion of ejection and sweep events does not change significantly with Mach number, the intensity of these events decreases with increasing compressibility. It is also found that particles tend to distribute in high-density regions and compressed region where the dilatation is negative. This is more evident near the wall. The joint distributions of the conditional streamwise velocity fluctuation and the dilatation at particle position indicate that it is the combination of these two mechanisms that gives rise to the reduced preferential concentration at high Mach number. As a result of the elongated conditional coherent structures, the scales of particle streaks increase with increasing Mach number.

Several issues remain in the present study. The gravity and lift forces are not taken into account, which may remarkably affect the preferential distribution and accumulation of particles. The Reynolds number and Mach number are not high enough to capture the multi-scale particle streaks and the high compressibility effects. The numerical simulations are limited in low volume and mass loading ranges. Two- and four-way coupling simulations at high Reynolds and Mach numbers are necessary in the future to validate the universality of concentration scaling relationships and reveal the interaction and the underlying mechanisms of compressible multiphase turbulence.

ACKNOWLEDGMENTS

The authors acknowledge the National Natural Science Foundation of China (Grants No. 12388101, No. 92052202, and No. 12072138).

[1] S. Balachandar and J. K. Eaton, Turbulent dispersed multiphase flow, Annu. Rev. Fluid Mech. **42**, 111 (2010).
[2] X. Li and B. Bai, Motion of submicron particles in a supersonic laminar boundary layer under hypergravity, Procedia Eng. **102**, 1193 (2015).
[3] J. Urzay, Turbulent dispersed multiphase flow, Annu. Rev. Fluid Mech. 2022, 593 (2018).
[4] T. Nagata, T. Nonomura, S. Takahashi, Y. Mizuno, and K. Fukuda, Direct numerical simulation of flow around a heated/cooled isolated sphere up to a Reynolds number of 300 under subsonic to supersonic conditions, Int. J. Heat Mass Transfer **120**, 284 (2018).
[5] P. J. Huffman and P. A. Haines, Visibility in heavy precipitation and its use in diagnosing high rainfall rates, AIAA J. **05**, 41 (1984).
[6] G. Palmer, E. Ching, M. Ihme, D. Allofs, and A. Gülhan, Modeling heat-shield erosion due to dust particle impacts for martian entries, J. Spacecr. Rockets **57**, 857 (2020).
[7] E. J. Ching, S. R. Brill, M. Barnhardt, and M. Ihme, A two-way coupled Euler-Lagrange method for simulating multiphase flows with discontinuous Galerkin schemes on arbitrary curved elements, J. Comput. Phys. **405**, 109096 (2020).
[8] P. Wang, J. Li, and X. Zheng, The effect of gravity on turbulence modulation in particle-laden horizontal open channel flow, Phys. Fluids **33**, 083315 (2021).
[9] Y. Yang, J. Wang, Y. Shi, Z. Xiao, X. T. He, and S. Chen, Interactions between inertial particles and shocklets in compressible turbulent flow, Phys. Fluids **26**, 091702 (2014).
[10] X. Li and B. Bai, Motion of submicron particles in supersonic laminar boundary layers, AIAA J. **53**, 1037 (2015).
[11] L. Brandt and F. Coletti, Annual review of fluid mechanics particle-laden turbulence: Progress and perspectives, Annu. Rev. Fluid Mech. **54**, 159 (2022).
[12] L.-P. Wangt and M. R. Maxey, Settling velocity and concentration distribution of heavy particles in homogeneous isotropic turbulence, J. Fluid Mech. **256**, 21 (1993).
[13] D. Kaftori, G. Hetsroni, and S. Banerjee, Particle behavior in the turbulent boundary layer. I. Motion, deposition, and entrainment, Phys. Fluids **7**, 1095 (1995).
[14] C. Marchioli, A. Giusti, M. V. Salvetti, and A. Soldati, Direct numerical simulation of particle wall transfer and deposition in upward turbulent pipe flow, Int. J. Multiphase Flow **29**, 1017 (2003).
[15] F. Picano, G. Sardina, and C. M. Casciola, Spatial development of particle-laden turbulent pipe flow, Phys. Fluids **21**, 093305 (2009).
[16] Y. Pan and S. Banerjee, Numerical simulation of particle interactions with wall turbulence, Phys. Fluids **8**, 2733 (1996).
[17] G. Sardina, F. Picano, P. Schlatter, L. Brandt, and C. M. Casciola, Statistics of particle accumulation in spatially developing turbulent boundary layers, Flow, Turbul. Combust. **92**, 27 (2014).
[18] M. Bernardini, Reynolds number scaling of inertial particle statistics in turbulent channel flows, J. Fluid Mech. **758**, R1 (2014).
[19] Z. Xia, Y. Shi, Q. Zhang, and S. Chen, Modulation to compressible homogenous turbulence by heavy point particles. I. Effect of particles' density, Phys. Fluids **28**, 016103 (2016).
[20] Q. Dai, K. Luo, J. Fan, Z. Guo, and Z. Chen, Fluctuations of thermodynamic variables in compressible isotropic turbulence laden with inertial particles, Phys. Fluids **33**, 093312 (2021).
[21] K. D. Squires and J. K. Eaton, Preferential concentration of particles by turbulence, Phys. Fluids A **3**, 1169 (1991).
[22] M. Caporaloni, F. Tampieri, F. Trombetti, and O. Vittori, Transfer of particles in nonisotropic air turbulence, J. Atmos. Sci. **32**, 565 (1975).
[23] M. W. Reeks, The transport of discrete particles in inhomogeneous turbulence, J. Aerosol Sci. **14**, 729 (1983).
[24] C. Marchioli and A. Soldati, Mechanisms for particle transfer and segregation in a turbulent boundary layer, J. Fluid Mech. **468**, 283 (2002).
[25] D. P. Sikovsky, Singularity of inertial particle concentration in the viscous sublayer of wall-bounded turbulent flows, Flow Turbul. Combust. **92**, 41 (2014).

[26] W. Xiao, T. Jin, K. Luo, Q. Dai, and J. Fan, Eulerian-lagrangian direct numerical simulation of preferential accumulation of inertial particles in a compressible turbulent boundary layer, J. Fluid Mech. **903**, A19 (2020).

[27] Q. Zhang, H. Liu, Z. Ma, and Z. Xiao, Preferential concentration of heavy particles in compressible isotropic turbulence, Phys. Fluids **28**, 055104 (2016).

[28] J. Bec, Fractal clustering of inertial particles in random flows, Phys. Fluids **15**, L81 (2003).

[29] J. Bec, L. Biferale, G. Boffetta, M. Cencini, S. Musacchio, and F. Toschi, Lyapunov exponents of heavy particles in turbulence, Phys. Fluids **18**, 091702 (2006).

[30] J. Bec, L. Biferale, M. Cencini, A. Lanotte, S. Musacchio, and F. Toschi, Heavy particle concentration in turbulence at dissipative and inertial scales, Phys. Rev. Lett. **98**, 084502 (2007).

[31] A. D. Bragg and L. R. Collins, New insights from comparing statistical theories for inertial particles in turbulence: I. Spatial distribution of particles, New J. Phys. **16**, 055013 (2014).

[32] S. Pedinotti, G. Mariotti, and S. Banerjee, Direct numerical simulation of particle behaviour in the wall region of turbulent flows in horizontal channels, Int. J. Multiphase Flow **18**, 927 (1992).

[33] J. Lee and C. Lee, Modification of particle-laden near-wall turbulence: Effect of Stokes number, Phys. Fluids **27**, 023303 (2015).

[34] T. Berk and F. Coletti, Transport of inertial particles in high-Reynolds-number turbulent boundary layers, J. Fluid Mech. **903**, A18 (2020).

[35] G. Sardina, F. Picano, P. Schlatter, L. Brandt, and C. M. Casciola, Large scale accumulation patterns of inertial particles in wall-bounded turbulent flow, Flow, Turbul. Combust. **86**, 519 (2011).

[36] G. Sardina, P. Schlatter, L. Brandt, F. Picano, and C. M. Casciola, Wall accumulation and spatial localization in particle-laden wall flows, J. Fluid Mech. **699**, 50 (2012).

[37] G. Wang and D. H. Richter, Two mechanisms of modulation of very-large-scale motions by inertial particles in open channel flow, J. Fluid Mech. **868**, 538 (2019).

[38] Y. Jie, Z. Cui, C. Xu, and L. Zhao, On the existence and formation of multi-scale particle streaks in turbulent channel flows, J. Fluid Mech. **935**, A18 (2022).

[39] M. Lagha, J. Kim, J. D. Eldredge, and X. Zhong, Near-wall dynamics of compressible boundary layers, Phys. Fluids **23**, 065109 (2011).

[40] B. Ganapathisubramani, N. T. Clemens, and D. S. Dolling, Large-scale motions in a supersonic turbulent boundary layer, J. Fluid Mech. **556**, 271 (2006).

[41] A. D. Marco, R. Camussi, M. Bernardini, and S. Pirozzoli, Wall pressure coherence in supersonic turbulent boundary layers, J. Fluid Mech. **732**, 445 (2013).

[42] P. Bechlars and R. D. Sandberg, Variation of enstrophy production and strain rotation relation in a turbulent boundary layer, J. Fluid Mech. **812**, 321 (2017).

[43] L. Duan, I. Beekman, and M. P. Martín, Direct numerical simulation of hypersonic turbulent boundary layers. Part 3. Effect of Mach number, J. Fluid Mech. **672**, 245 (2011).

[44] L. Duan, I. Beekman, and M. P. Martín, Direct numerical simulation of hypersonic turbulent boundary layers. Part 2. Effect of wall temperature, J. Fluid Mech. **655**, 419 (2010).

[45] Q. Dai, T. Jin, K. Luo, and J. Fan, Direct numerical simulation of particle dispersion in a three-dimensional spatially developing compressible mixing layer, Phys. Fluids **30**, 113301 (2018).

[46] J. R. Fessler, J. D. Kulick, and J. K. Eaton, Preferential concentration of heavy particles in a turbulent channel flow, Phys. Fluids **6**, 3742 (1994).

[47] E. J. Teh and C. T. Johansen, Effect of particle momentum transfer on an oblique-shock-wave/laminar-boundary-layer interaction, Acta Astronaut. **128**, 431 (2016).

[48] X. Li, Y. Ma, and D. Fu, DNS and scaling law analysis of compressible turbulent channel flow, Phys. Sci. China A **44**, 645 (2001).

[49] L. Xinliang, F. Dexun, and M. Yanwen, Direct numerical simulation of compressible isotropic turbulence, Phys. Sci. China A **45**, 1452 (2002).

[50] X.-L. Li, D.-X. Fu, and Y.-W. Ma, Direct numerical simulation of a spatially evolving supersonic turbulent boundary layer at $Ma = 6$, Chin. Phys. Lett. **23**, 1519 (2006).

[51] W. Sutherland, LII. The viscosity of gases and molecular force, London Edinburgh Dublin Philos. Mag. J. Sci. **36**, 507 (1893).

[52] Y. Morinishi, S. Tamano, and K. Nakabayashi, Direct numerical simulation of compressible turbulent channel flow between adiabatic and isothermal walls, J. Fluid Mech. **502**, 273 (2004).
[53] A. Harten, High resolution schemes for hyperbolic conservation laws, J. Comput. Phys. **49**, 357 (1983).
[54] C.-W. Shu and S. Osher, Efficient implementation of essentially non-oscillatory shock-capturing schemes, J. Comput. Phys. **77**, 439 (1988).
[55] D. S. Balsara and C. W. Shu, Monotonicity preserving weighted essentially non-oscillatory schemes with increasingly high order of accuracy, J. Comput. Phys. **160**, 405 (2000).
[56] J. Yao and F. Hussain, Turbulence statistics and coherent structures in compressible channel flow, Phys. Rev. Fluids **5**, 084603 (2020).
[57] K. Hadinoto, E. N. Jones, C. Yurteri, and J. S. Curtis, Reynolds number dependence of gas-phase turbulence in gas-particle flows, Int. J. Multiphase Flow **31**, 416 (2005).
[58] Y. Ling, M. Parmar, and S. Balachandar, A scaling analysis of added-mass and history forces and their coupling in dispersed multiphase flows, Int. J. Multiphase Flow **57**, 102 (2013).
[59] L. Schiller and A. Naumann, Fundamental calculations in gravitational processing, Z. Ver. Dtsch. Ing. **77**, 318 (1933).
[60] E. Loth, Compressibility and rarefaction effects on drag of a spherical particle, AIAA J. **46**, 2219 (2008).
[61] T. Zhou, L. Zhao, W. Huang, and C. Xu, Non-monotonic effect of mass loading on turbulence modulations in particle-laden channel flow, Phys. Fluids **32**, 043304 (2020).
[62] E. R. V. Driest, Turbulent boundary layer in compressible fluids, J. Aeronaut. Sci. **18**, 145 (1951).
[63] L. H. Shendalman, Boundary layers of flow and temperature, Alfred Walz, the Massachusetts Institute of Technology Press, Cambridge, Massachusetts (1969), AIChE J. **16**, 338 (1970).
[64] S. Pirozzoli, F. Grasso, and T. B. Gatski, Direct numerical simulation and analysis of a spatially evolving supersonic turbulent boundary layer at $\mathrm{M} = 2.25$, Phys. Fluids **16**, 530 (2004).
[65] Y. S. Zhang, W. T. Bi, F. Hussain, and Z. S. She, A generalized Reynolds analogy for compressible wall-bounded turbulent flows, J. Fluid Mech. **739**, 392 (2014).
[66] D. Modesti and S. Pirozzoli, Reynolds and Mach number effects in compressible turbulent channel flow, Int. J. Heat Fluid Flow **59**, 33 (2016).
[67] X. Liang and X. Li, Direct numerical simulation on Mach number and wall temperature effects in the turbulent flows of flat-plate boundary layer, Commun. Comput. Phys. **17**, 189 (2015).
[68] Q. Dai, K. Luo, T. Jin, and J. Fan, Direct numerical simulation of turbulence modulation by particles in compressible isotropic turbulence, J. Fluid Mech. **832**, 438 (2017).
[69] G. N. Coleman and J. Kim, A numerical study of turbulent supersonic isothermal-wall channel flow, J. Fluid Mech. **305**, 159 (1995).
[70] M. Yu, C.-X. Xu, and S. Pirozzoli, Genuine compressibility effects in wall-bounded turbulence, Phys. Rev. Fluids **4**, 123402 (2019).
[71] K. T. Christensen and R. J. Adrian, Statistical evidence of hairpin vortex packets in wall turbulence, J. Fluid Mech. **431**, 433 (2001).
[72] R. J. Adrian, On the role of conditional averages in turbulence theory, Turbul. Liq. **1**, 323 (1977).
[73] D. H. Richter and P. P. Sullivan, Modification of near-wall coherent structures by inertial particles, Phys. Fluids **26**, 103304 (2014).
[74] J. Zhou, R. J. Adrian, S. Balachandar, and T. M. Kendall, Mechanisms for generating coherent packets of hairpin vortices in channel flow, J. Fluid Mech. **387**, 353 (1999).